

# The angular separation of the components of the Cepheid AW Per<sup>★</sup>

D. Massa<sup>1†</sup> and N. R. Evans<sup>2†</sup>

<sup>1</sup>*SGT, Inc., NASA's GSFC, Code 665, Greenbelt, MD 20771, USA*

<sup>2</sup>*Center for Astrophysics, 60 Garden Street, MS 4, Cambridge, MA 02138, USA*

Accepted 2007 September 25. Received 2007 September 21; in original form 2007 August 8

## ABSTRACT

The 6.4 d classical Cepheid AW Per is a spectroscopic binary with a period of 40 yr. Analysing the centroids of *Hubble Space Telescope*/Space Telescope Imaging Spectrograph (*HST*/STIS) spectra obtained in 2001 November, we have determined the angular separation of the binary system. Although we currently have spatially resolved data for a single epoch in the orbit, the success of our approach opens the possibility of determining the inclination,  $\sin i$ , for the system if the measurements are repeated at additional epochs. Since the system is potentially a double lined spectroscopic binary, the combination of spectroscopic orbits for both components and the visual orbit would give the distance to the system and the masses of its components, thereby providing a direct measurement of a Cepheid mass.

**Key words:** binaries: spectroscopic – binaries: visual – stars: individual: AW Per – Cepheids.

## 1 INTRODUCTION

Cepheids are important stars in many respects, most notably for their roles as fundamental rungs on the cosmic distance ladder and the challenges their structure pose to stellar interiors modelling. The use of Cepheids as primary extragalactic distance indicators makes a quantitative understanding of their properties extremely valuable. While the Magellanic Clouds are perhaps the best laboratory to study Cepheids, the dependence of the period–luminosity relation on metallicity is still not fully understood (Romaniello et al. 2005). Consequently, accurate distances (absolute magnitudes) to Galactic Cepheids are needed to fully understand and quantify this dependence and to apply Cepheid scale to more metal-rich spiral galaxy stars which are more commonly used in extragalactic distance determinations.

Cepheids also present important tests for interiors calculations since, as evolved stars, their structure is dictated by their evolutionary history. In addition, the models must predict the pulsational properties of Cepheids, making the modelling especially challenging. This complexity is codified in the term ‘the Cepheid mass problem’. 40 years ago, when the first hydrodynamic pulsation calculations were made, it was realized that the mass could be derived by either matching the Herzprung progression of secondary maxima or by a parametrization of the pulsation constant. These masses were as much as a factor of 2 smaller than evolutionary calculations. A

reconciliation was recently achieved from re-evaluation of the interior opacities (see Simon 1990, for a summary). We see, therefore, that in addition to absolute magnitudes, obtaining accurate Cepheid masses is also important.

If we can determine the angular separations of binary systems containing a Cepheid, which are double lined spectroscopic binaries (SB2s), then the distances and masses of the Cepheids can be derived from basic physics. Because of the central roles of Cepheids in fundamental astrophysics, it is important to have such direct measurements. While several Cepheid distances have been measured directly by the *Hipparcos* satellite, the quality of these measurements was only sufficient for statistical considerations (e.g. Groenewegen & Oudmaijer 2000). More recently, a large campaign using the Fine Guidance Sensor on *Hubble Space Telescope* (*HST*) has begun to yield accurate distances to single Cepheids (Benedict et al. 2002). However, to date the mass of only one Cepheid, Polaris, has been directly determined from fundamental observations (Evans et al. 2007).

Although SB2s containing a Cepheid and an A or B star are common (see Evans 1995), these stars are difficult to resolve in the optical. This is because of the inevitable, enormous magnitude differences of the components in the optical, which result from massive stars evolving toward cooler temperatures at nearly constant luminosity. The top panel of Fig. 1 shows a typical example of a Cepheid + B star binary, and the contrast between the primary and secondary throughout the optical and infrared (IR) is obvious.

Thus, while the measurement of a Cepheid mass by directly imaging a SB2 with a Cepheid primary and an A or B star secondary has been a long-sought goal, ground-based studies have not, as yet, been able to accomplish this (even though they have been able to resolve the stellar discs of some Cepheids; e.g. Kervella et al. 2004, and references therein). As a result, indirect methods have been developed to determine the masses of Cepheids. The most popular of these uses

<sup>★</sup>Based on observations with the NASA/ESA *Hubble Space Telescope*, obtained at the Space Telescope Science Institute, which is operated by the Association of Universities for Research in Astronomy, Inc. under NASA contract No. NAS5-26 555.

†E-mail: massa@derckmassa.net (DM); evans@head-cfa.harvard.edu (NRE)

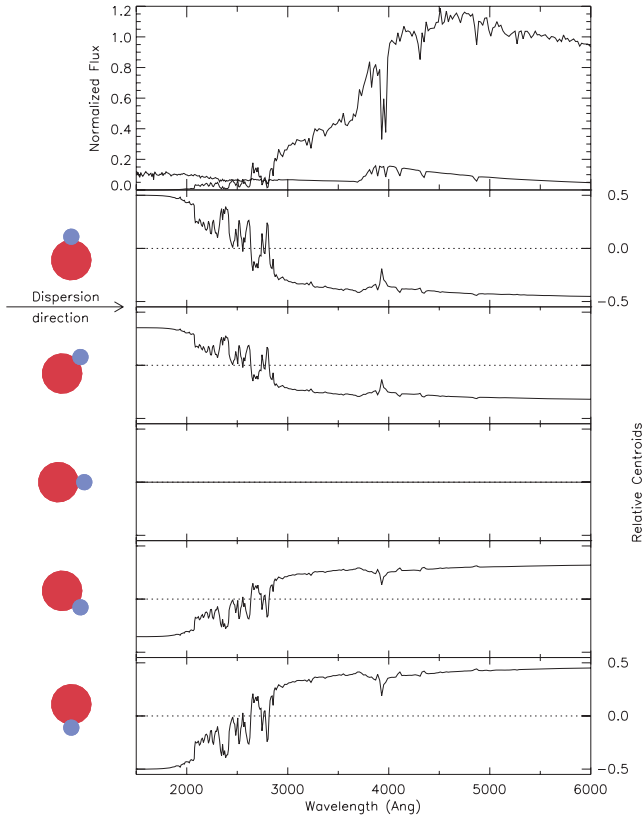


**Figure 1.** Kurucz models for a typical Cepheid (large/red) + hot star (small/blue) binary. The top panel shows how the secondary is roughly 10 times fainter in the optical, making the system extremely difficult to resolve from the ground. On the other hand, the secondary dominates the flux from the system in the UV. The remaining five panels demonstrate how the wavelength dependence of the spectrum centroid changes with orientation of the axis of the binary relative to the dispersion for five different orientations, shown to the left of each panel. Notice that in the spectral region accessible from the ground, the centroid shifts by less than 10 per cent of the full separation. The ‘crossover’ point is not reached until  $\lambda \sim 2500 \text{ \AA}$ . A colour version of the figure is available in the electronic version of the paper.

a combination of ultraviolet (UV) and optical spectroscopy to obtain radial velocity curves for both components. Then the UV spectral energy distribution (SED) of the hot secondary is used to obtain its temperature. Finally, the mass–temperature relation for main-sequence A or B stars is used to infer the mass of the secondary and, thus (since the system is an SB2), the mass of the primary. This approach has been applied to several systems (SU Cyg, S Mus and V350 Sgr), using *International Ultraviolet Explorer* (IUE) or *HST* spectra to determine the radial velocity curves and SEDs of the secondary (Evans et al. 1998). The masses obtained by this approach agree, on average, with the mass–luminosity predictions from evolutionary calculations with moderate convective overshoot (e.g. Schaller et al. 1992). However, this approach requires an exact understanding of the evolutionary phase of the hot secondary and relies on its spectroscopic parallax to determine the distances to the systems. Clearly, a direct measurement of the masses of both components is more desirable.

In this paper, we describe how we used the Space Telescope Imaging Spectrograph (STIS) on *HST* to resolve the potential SB2 Cepheid binary AW Per using an approach we call ‘cross-dispersion imaging’. AW Per is a 6.4 d Cepheid which is in a roughly 40 yr orbit

with its hot secondary (Evans, Vinko & Wahlgren 2000). Evans (1989) studied the system and determined that the secondary is a main-sequence B7–8 star and that the colour excess of the system is  $E(B - V) = 0.52$ . The  $T_{\text{eff}}$  of the secondary is expected to be  $\sim 12\,000 \text{ K}$  (Evans 1994).

The remainder of the paper is organized as follows: Section 2 provides an overview the approach used to ‘resolve’ the binary; Section 3 describes the observations; Section 4 gives the data analysis; Section 5 details the analysis of the observations; Section 6 presents the results; Section 7 discusses the results and their implications and Section 8 summarizes the findings.

## 2 THE APPROACH (CROSS-DISPERSION IMAGING)

### 2.1 Basic principles

Massa & Endal (1987) describe how combining imaging and spectroscopy can dramatically increase the effective ‘resolving power’ of an instrument. Specifically, they showed how the wavelength dependence of the centroid of a spectrum can determine the angular separation of an unresolved binary whose components have distinctly different spectra. The basic concept of this approach is quite simple. It is based on an idea put forth by Beckers (1982) and has been independently discovered by a number of others (see e.g. Porter, Oudmaijer & Baines 2004, and references therein).

Like all cross-dispersion imaging techniques, some sort of a model is required to interpret the observations. This model might be extremely simple, as in the case of a binary where one assumes that the system is composed of exactly two stars, and that one contributes all of the flux at one wavelength and the other contributes all of the flux at another wavelength. This crude model would be sufficient to ‘resolve’ the binary from the properties of its spectrum.

Consider the image of a highly unresolved binary system. To first order, the image of the combined light from the system is indistinguishable from a point source. However, the position of an image at any given wavelength will be displaced toward the location of the binary component which contributes most of the light that wavelength. In principle, one could obtain images at several different wavelengths and determine how the centres of the images shift from one exposure to the next. Analysis of this set of data (along with a model for the flux ratios in each band) would then determine the separation of the two components (Beckers 1982). The drawback of this direct approach is that all of the exposures would have to be obtained using different optical elements, making alignment at the subpixel level effectively impossible. Instead, Massa & Endal (1987) show that tracking the centroid of the spectrum of the binary has the same effect. Furthermore, because all of the position measurements (the centroid of the spectrum at each wavelength) are obtained at one time, this method is more efficient and the measurements are differential in nature, freeing them from several sources of systematic error.

To make these notions quantitative, let  $x$  and  $y$  be the angular coordinates on the detector which are parallel and perpendicular to the wavelength dispersion. Therefore, the wavelengths,  $\lambda$ , are given by  $\lambda = \lambda(x)$ . Now, consider a binary whose components have an angular separation  $\theta$  and photon fluxes per unit wavelength  $N_p(\lambda)$  and  $N_s(\lambda)$  for the primary and secondary, respectively. Further, let  $\phi$  be the position angle of the binary on the sky [measured counter-clockwise (c.c.) from north toward east of a line from the primary to the secondary] and let  $\alpha$  be a similarly measured angle between north and a line in the dispersion direction pointing in the direction

of decreasing wavelength. Thus,  $\alpha$  can be varied by changing the orientation of the telescope. With these definitions, the wavelength dependence of the centroid of the spectrum of a single observation of a binary is

$$y(\lambda) = \frac{\Delta y}{1 + N_p(\lambda)/N_s(\lambda)} + \text{const.}, \quad \text{where} \quad (1)$$

$$\Delta y = \theta \sin(\phi - \alpha) \quad (2)$$

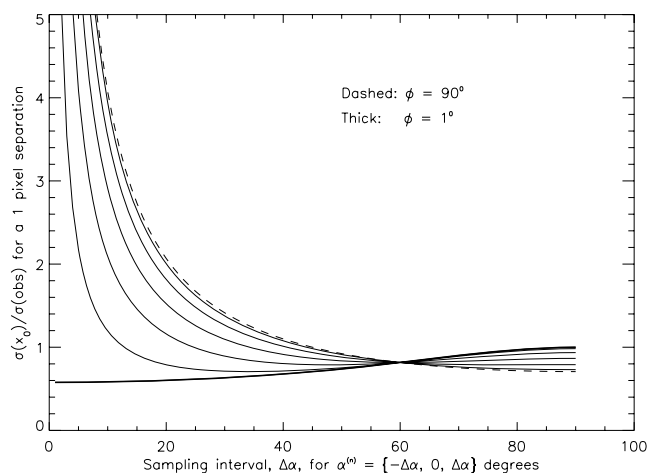
(see Appendix A). Thus, if  $N_p(\lambda)/N_s(\lambda)$  is known, then measurements at two or more orientations ( $\alpha$ s) enables one to determine  $\theta$  and  $\phi$ , the separation and position angle of the binary. Note that if the SEDs of the components are vastly different, then the position of the centroid shifts from one to the other, depending upon which star dominates the flux at each wavelength. On the other hand, if the binary components have identical SEDs, then no spatial information can be gained from the centroid positions.

Fig. 1 is a cartoon depicting how the centroid of the spectrum of a binary star, whose components have very different effective temperatures, is influenced by the relative energy distributions of the two components and the orientation of the binary relative to the dispersion direction of a spectrograph. In this case, the centroid shifts from the cool component at long wavelengths to the hot component at short wavelengths. We define the crossover wavelength as that wavelength where each binary component contributes equally to the flux. For Cepheid binaries, this wavelength is typically in the near UV ( $\sim 3000 \text{ \AA}$  for the case shown). In order to infer spatial information from the centroids, it is desirable to span as large a wavelength baseline as possible, to maximize the deflections in the centroid positions. The best case would be to cover a large enough wavelength range with a single setting, so that one end of the spectrum is totally dominated by one star and the other end is dominated by the other. If this is not practical, a wavelength band centred on the crossover wavelength and covering a baseline large enough to experience more than a 50 per cent centroid deflection is adequate. However, in this case, one needs an estimate of the SEDs of the two binary components in order to extract the angular separation. Note that if the absolute flux calibration of the instrument is well determined, then the flux observations can provide additional information which can be incorporated into the determination of the angular separation (see Section 5).

Finally, to unambiguously determine the separation and position angle of the binary, two or more observations are required in order to solve equation (2) for  $\theta$  and  $\phi$  in terms of the measured quantities  $\Delta y^{(n)}$  and  $\alpha^{(n)}$ , for  $n \geq 2$ .

The final error associated with the angular separation and the position angle measurements depends upon the bandpass of the observation, the signal-to-noise ratio of the data (discussed in the next section), the number of independent orientations obtained and the relation between these angles and  $\phi$ . We have examined the relative error for sampling three orientations,  $\alpha^{(n)} = \{-\Delta\alpha, 0, +\Delta\alpha\}$ , for position angles between  $1^\circ$  and  $90^\circ$ . Fig. 2 demonstrates how the relative accuracy of the observations changes as a function of sampling interval,  $\Delta\alpha$ , and relative orientations,  $\phi$ , for this case. For most orientations, any sampling with  $\Delta\alpha \gtrsim 30^\circ$  provides comparable accuracy.

The approximations developed in this section are only valid in the sub-Rayleigh regime. Once the sources are resolved at any wavelength, the entire image must be modelled using an accurate representation of the point spread function as well as the fluxes of the two objects.



**Figure 2.** Relative error in the angular separation of a binary determined from fitting a cosine curve to measurements obtained at three orientations,  $\{-\Delta\alpha, 0, +\Delta\alpha\}$  versus  $\Delta\alpha$  (abscissa) over the interval  $\Delta\alpha = 1^\circ \rightarrow 90^\circ$ . The different curves are for different values of the orientation of the system on the sky,  $\phi$ , between  $\phi = 1^\circ \rightarrow 90^\circ$ .

## 2.2 Exposure times and random errors

The counts needed to centroid to an accuracy  $\sigma[y(\lambda)]$  can be estimated for an instrument whose spread function perpendicular to the dispersion is a Gaussian with full width at half-maximum (FWHM) =  $\xi$ . A single count is equivalent to one estimate of the centre of the spectrum drawn from a sample with an rms dispersion  $\sigma = \xi/\sqrt{8 \ln 2} = 0.42\xi$ . Therefore,  $N$  samples (counts) determine the centroid to an accuracy of

$$\sigma[y(\lambda)] = \frac{0.42\xi}{\sqrt{N(\lambda)}}. \quad (3)$$

Equation (3) gives the counts needed over a wavelength band to obtain the desired accuracy. The FWHM of the STIS PSF varies from  $\sim 0.05$  to  $0.07$  arcsec (depending on wavelength) and the minimum number of counts obtained in one 10-min observation over a spectral resolution element (2 pixel) was 4000, and we obtained three of these. Therefore, the poorest precision we can expect based upon simple sampling arguments is  $\sim 3 \times 10^{-4}$  arcsec, and this is for a single resolution element. In all, there are 512 independent resolution elements which will be combined to determine a single measurement of  $\Delta y$  through the use of equation (1). Therefore, random noise in the angular separation determinations should be  $\lesssim 10^{-4}$  arcsec, and not a limiting factor for our observations. However, as is typical for most observations, we shall see that systematic effects will dominate the error budget (see Section 4).

## 3 THE OBSERVATIONS

As can be seen from the top panel of Fig. 1, a broad wavelength baseline is needed to optimize the extraction process. Furthermore, good spectral resolution is also advantageous, since spectral features provide additional constraints. Consequently, we employed the STIS on *HST* to obtain high spatial resolution, excellent wavelength coverage and good spectral resolution. We used the STIS NUV-MAMA detector together with its G230L grating, since this combination provided good coverage ( $1600 \leq \lambda \leq 3160 \text{ \AA}$ ) of the expected crossover point (see Kim Quijano et al. 2003).

Spectra were obtained at three distinct roll angles (see Table 1) which differ by  $\sim \pm 20^\circ$ . Although rolls of  $\pm 60^\circ$  would be optimal,

**Table 1.** Observation log.

Obs ID	Offset (arcsec)	Roll ( $^{\circ}$ )	Obs date (MJD 52235)	Exp. time (min)	Phase <sup>a</sup> $\Phi$	V (mag)	(B – V) (mag)
o6f104010	+0.0	175.526	0.34765625	10.0	0.906	7.40	1.02
o6f104020	+0.1	175.526	0.35546875	10.0	0.907	7.39	1.01
o6f104020	–0.1	175.526	0.36328125	11.4	0.909	7.38	1.01
o6f105010	+0.0	205.000	0.41406250	10.0	0.916	7.34	1.00
o6f105020	+0.1	205.000	0.42187500	10.0	0.918	7.33	0.99
o6f105030	–0.1	205.000	0.42968750	11.4	0.919	7.32	0.99
o6f106010	+0.0	146.526	0.48046875	10.0	0.927	7.27	0.97
o6f106020	+0.1	146.526	0.48828125	10.0	0.928	7.26	0.97
o6f106030	–0.1	146.526	0.49609375	11.4	0.929	7.26	0.97

<sup>a</sup>Phase, V and (B – V) are derived from sources in the literature, as discussed in the text.

we were limited to smaller rolls by *HST* restrictions for objects at the declination of AW Per. Although not optimal, Fig. 2 shows that this restricted range does not sacrifice very much in theoretical accuracy. After a standard STIS target acquisition, which centres the binary within a 0.1-arcsec aperture, we obtained the science observations through the 25MAMA aperture, which provides slitless spectra of the binary. At each roll, we offset the star by  $\pm 0.1$  arcsec and obtained additional science exposures. This procedure allows us to characterize localized distortions in the detector. It is also useful for determining the sensitivity of the observations to their position on the detector, since each spectrum is sampled differently by the pixel lattice. Since the spectrum was repositioned to within 2 pixel ( $< 0.05$  arcsec) after each roll, the dispersion of measurements obtained at the  $\pm 0.1$  arcsec offsets should provide a good characterization of the errors that result from all of the changes encountered in the positioning of the spectrum. The reproducibility of these observations also provides a more realistic measurement of the centroiding errors than those based on simple signal-to-noise ratio considerations. As a result of our observing strategy, we obtained three observations at each of three rolls, for a total of nine spectra, with exposure times of roughly 10 min each.

The orientations mentioned above are measured with respect to the STIS coordinate system, which we define as the  $x_0$ – $y_0$  system. In this system, the dispersion direction (from red to blue) makes an angle (measured in the c.c. direction) of  $-1^{\circ}.4$  with the  $x_0$  axis.

## 4 DATA REDUCTION

### 4.1 Centroids

The first step in the reduction process was to extract the centroids. This presents a problem, since the STIS detector does not oversample the *HST* PSF. However, since (as will be explained shortly) only relative centroids will be needed, we can accept some level of bias in the extraction process, as long as it is consistent. This is because the ultimate measurements will be differences of the centroids, which will cancel small, uniform biases introduced in the extraction process.

We used three separate approaches to extract the centroids,  $y(\lambda)$ , from the raw images. We chose to analyse the raw images (in their native ‘highres’  $2048 \times 2048$  format) because initial experimentation showed that the geometrically corrected images did little to improve the relative positions of the centroids over the range of 10 pixel or less (which are the scales important to us). Thus it was felt best to avoid the inevitable smoothing which is introduced by the resampling involved in geometric corrections.

The first approach we used was a simple cross-correlation technique relative to a set of 0.025 arcsec FWHM Gaussians. The second one employed a standard cross-correlation technique using the cross-dispersion profiles of a spectrum of a standard star (the white dwarf GD71) which was observed at roughly the same position on the detector with the same grating. We used sinc interpolation in the cross-correlation to compensate for the undersampling of the PSF by the MAMA detector. Finally, we used a non-linear least squares fit to a set of Gaussians whose FWHMs, central positions and amplitudes were allowed to vary at each pixel. No systematic differences were found among all three approaches. However, the results from the non-linearly extracted centroids produced the results with the lowest pixel-to-pixel scatter, and these were adopted for the following analysis.

The three sets of centroid measurements at each roll angle were rebinned to 512 elements from the 2048 elements available in the raw images, and these were used to construct mean centroids at each roll and their standard deviations. Because the centroids near the edges of the detector are poorly determined, of the 512 binned pixels (in the wavelength direction) only about 490 are well behaved. The standard deviations for these 490 pixel determined for each roll angle are overplotted as a function of wavelength in Fig. 3. The rms means for each roll angle are 0.027, 0.024 and 0.027 pixel or (0.67, 0.59 and 0.67 mas). Remember, these are the single observation standard deviations for a single pixel, and there are nine independent

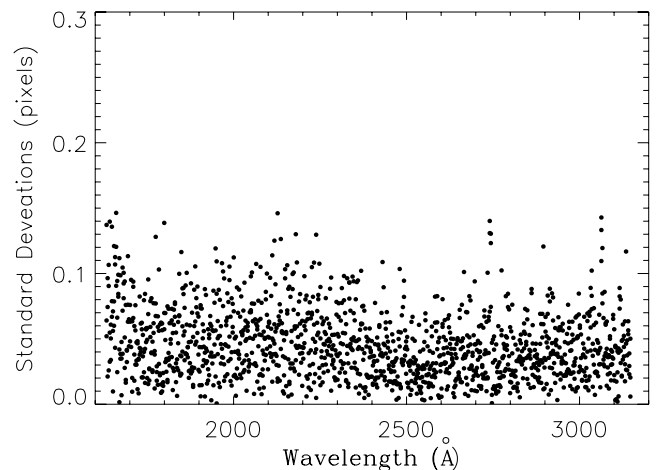


**Figure 3.** Standard deviations of the three independent spectra of AW Per obtained at each roll angle. The standard deviations for each roll angle are overplotted.



observations with 490 useful pixels. Notice also that this scatter is significantly larger than the one expected from the simple signal-to-noise ratio arguments of the previous section. The reason is that the actual uncertainties are set by random differences between the photometric and geometric centroids of the pixels, and by localized geometric distortions in the detector over the range of a few pixels. Nevertheless, the repeatability of the centroids (to a few per cent of a pixel) is considered quite good, and we will use this scatter to characterize the actual measurement errors in the centroid positions.

Since the centroids are extracted from the raw images, they contain large-scale geometric distortions. Consequently, we will analyse the relative centroids. To construct these, we first combine the centroids determined at each offset for a particular roll angle to produce a mean centroid,  $\langle y \rangle$ , at each roll. These measurements contain geometric distortions and any systematic effects introduced by the centroid extraction technique. However, when we analyse the differences between each individual mean and the grand mean of all the observations, these systematic affects are removed. This is because the offsets at each roll are larger than the displacements from one roll to another, and the scatter that the former exhibit (Fig. 3) demonstrates that localized geometric distortions are small. Similarly, any systematic affects that result from mismatches between the actual PSF orthogonal to the dispersion and the Gaussian used to determine the centroids will cancel out, since the same process is used in each case.

Finally, we must account for the fact that  $y(\lambda)$  is not exactly perpendicular to the dispersion. As a result, we must divide the final displacements that we measure by  $\cos(1^\circ 4)$ .

## 4.2 Fluxes

STIS fluxes were extracted from the images using the CALSTIS IDL software package developed by Lindler (1998) for the STIS Instrument Definition Team. In order to constrain the B star flux contribution, we also incorporate the available *IUE* spectra (obtained when the Cepheid component was near minimum light), into the analysis given in Section 5. The *IUE* fluxes were placed upon the *HST*/STIS flux system using the transformations described by Massa & Fitzpatrick (2000). Fig. 4 compares the *IUE* and STIS spectra. It is immediately clear that the *IUE* long wavelength spectra were obtained when the Cepheid was near minimum light ( $\Phi = 0.53$ ; Evans 1989), while the STIS observations were near maximum light (Table 1).

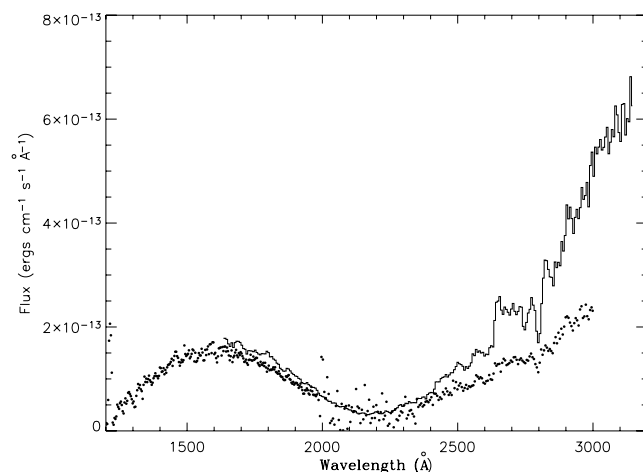


**Figure 4.** Plots of the mean STIS spectrum of AW Per (solid curve) together with the available *IUE* spectra (dotted), calibrated to the *HST* flux system.

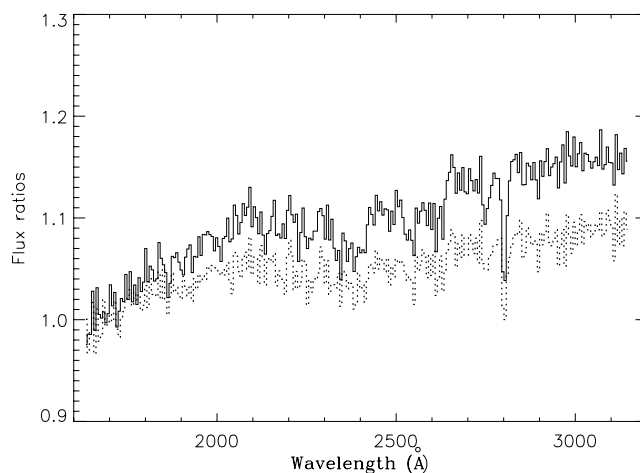


**Figure 5.** Plots of the ratios of mean STIS spectra of AW Per obtained at the second and third roll angles divided by the mean flux obtained at the first roll angle. These plots demonstrate how the Cepheid component brightened over the 3.5 h observing sequence. Notice that the flux at the shortest wavelengths does not change, since it is dominated by the B star secondary.

The effects of extinction are also clearly apparent, as is the fact that the *IUE* fluxes are a factor of 1.146 smaller than the STIS fluxes. This discrepancy is a constant over the region of overlap, and its origin is unknown. Consequently, we cannot be certain which set of fluxes is correct. In Section 6 we show that this ambiguity introduces a significant uncertainty into our results.

The variability of the Cepheid is clearly detectable in the STIS spectra. Fig. 5 shows STIS flux ratios for the mean spectra obtained at the second and third roll angles divided by the first. The time lapsed between the mean observations is 1.59 and 3.19 h, respectively. This plot demonstrates two things. First, the Cepheid flux changed significantly throughout the three *HST* orbits spanned by the observations. Secondly, the flux ratios decrease with wavelength, becoming unity at the shortest wavelengths. This is contrary to what is normally seen in single Cepheids like  $\delta$  Cep (Schmidt & Parsons 1982) where the flux changes typically increase with decreasing wavelength. Consequently, this figure shows that the flux at the shortest wavelengths is dominated by the B star, which does not vary.

The following analysis also requires the colour and magnitude of the system and the time of the observations. We combined the data from Szabados (1980, 1991), Moffett & Barnes (1984) and Kiss (1998), using the period and HJD for zero phase from Kiss (1998). The combined data were fit with a high-order polynomial, and this was used to determine the *V* and (*B* − *V*) photometry at the times of the STIS observations. The resulting phases and photometry are listed in Table 1.

## 5 ANALYSIS

### 5.1 Overview

Because our spectra cover a limited bandpass, we require an estimate for the flux ratio of the binary components in order to extract the wavelength dependence of the centroids. This flux ratio is constrained, since it must also satisfy the observed flux of the system, which is the reddened, combined flux of the two binary components. Ideally, one would fit the observed flux and centroid positions with a combination of single star spectra obtained with the same

instrument and which experience the same reddening. However, because there is no such library of single star spectra available, we used an approach which employs a model for the B star SED and for the UV extinction to construct the combined flux and the centroids. We then used a non-linear least squares fitting procedure<sup>1</sup> to fit the centroids and fluxes simultaneously. This method is described in detail in Section 5.3.

## 5.2 Model components

We now describe the components of the model used to fit the observations. In a few instances, refinements might increase the accuracy, but in the interest of expediency, certain effects were ignored for the first attempt. First, we use Kurucz (1991) Atlas 9 models with updated metallicities<sup>2</sup> for the B star. We use only models with a microturbulent velocity of  $2.0 \text{ km s}^{-1}$ . The synthetic photometry for the models was calibrated as in Fitzpatrick & Massa (2005). We set  $\log g = 4.0$  for the B star atmosphere. The sensitivity of our results to this assumption is tested once a fit is achieved. The model atmosphere fluxes were prepared in the manner described by Fitzpatrick & Massa (2005), which is best suited to the *IUE* fluxes. The dust model is quite general. We use the Fitzpatrick (1999) formulation of the Fitzpatrick & Massa (1990) model since we need a representation of the near-UV extinction, and the original Fitzpatrick & Massa (1990) formulation does not provide one. Although the Fitzpatrick (1999) curve for the near-UV is largely untested, it is reasonable and the best currently available. To provide additional flexibility to the Fitzpatrick model, we allow the bump strength ( $c_3$ ), the width of the  $2175 \text{ \AA}$  ( $\gamma$ ) and far-UV curvature term ( $c_4$ ) to vary independently. In this way, we can accommodate any observed extinction curve. As a result, the  $R_V$  parameter (the ratio of visual extinction to colour excess) only affects the general slope of the UV extinction and the shape of the near-UV curve, and the wavelength dependence of the total extinction to an object can be expressed as

$$A_\lambda \equiv A[R_V, E(B - V), \gamma, c_3, c_4; \lambda]. \quad (4)$$

## 5.3 Details of the fitting procedures

We simultaneously fit the STIS centroids at all three roll angles and the *IUE* flux from the B star. We constrain the reddened model for the B star by assuming that all of the flux from the system for  $\lambda \leq 1650 \text{ \AA}$  is due to the B star. The difference between the observed flux and the reddened B star model provides the Cepheid SED which is used in fitting the centroids. The free parameters of the fit are the three  $\Delta y^{(n)}$  (displacements perpendicular to the dispersion at each roll angle),  $T_{\text{eff}}^s$  (the effective temperature of the B star secondary),  $[\text{m}/\text{H}]_s$  (the abundance parameter for the B star),  $E(B - V)$  (the colour excess of the system, consistent with the fluxes),  $R_V$  (which determines the slope of the UV extinction curve),  $\gamma$  (the width of the  $2175 \text{ \AA}$  bump),  $c_3$  (the bump strength) and  $c_4$  (the strength of the far UV curvature) – 10 parameters in all. The  $V$  magnitude of the B star,  $V_s$ , is fixed by the observed flux attributed to the B star at  $\lambda = 1650 \text{ \AA}$  and the extinction at that wavelength relative to  $V$ . In addition to the separations, the results also yield an empirical,

unreddened UV SED and photometry for the Cepheid. These can then be compared to models or to actual Cepheids. Since the derived Cepheid flux is identical to the observed flux minus the B star flux for wavelengths longward of  $1650 \text{ \AA}$ , the flux in this region is fit exactly. The equation used to fit the centroids is

$$y(\lambda)^{(n)} = \Delta y^{(n)} \left[ 1 + \frac{N(\lambda)_{\text{obs}}^{(n)} - \theta_s^2 N(T_s, \log g_s, v_t, [\text{m}/\text{H}]; \lambda)}{\theta_s^2 N(T_s, \log g_s, v_t, [\text{m}/\text{H}]; \lambda)} \right]^{-1} \quad (5)$$

and the unreddened flux of the Cepheid is given by

$$N(\lambda)_p^{(n)} = [N(\lambda)_{\text{obs}}^{(n)} - \theta_s^2 N(T_s, \log g_s, v_t, [\text{m}/\text{H}]; \lambda)] \times 10^{A[R_V, E(B - V), \gamma, c_3, c_4; \lambda]}, \quad (6)$$

where  $\theta_s$  is the angular diameter of the B star (fixed by the flux at  $1650 \text{ \AA}$ ) and  $n = 1, 2, 3$  represents the observations obtained at each roll angle, which are means of the data for the three offset positions. We cannot use a single mean for the fluxes, since significant changes in  $V$ ,  $(B - V)$  and the UV SED occur over the course of the observations (see Table 1, Fig. 5) and must be taken into account. However, the data were averaged at each roll, since the time between offsets was much smaller than the time between rolls.

A major advantage of our approach is that it only relies on a Kurucz Atlas 9 model for the B star, and recent work by Fitzpatrick & Massa (1999, 2005) has demonstrated that these provide excellent representations of low-resolution B star SEDs. Further, it avoids using the Atlas 9 models for the Cepheid component, which is desirable since the accuracy of Cepheid model atmospheres has not been fully tested, especially in the UV. This issue is addressed further in Section 6. The disadvantage of our approach is that we must have extremely well calibrated fluxes, and we have already seen an inconsistency between the poorly exposed *IUE* fluxes and the STIS data.

## 5.4 Determining the separations

The final step in the analysis is to fit the angular separations derived at each roll angle to a sine curve whose phase and amplitude are related to the position angle and separation of the binary (equation 2). The amplitude of the curve is the full separation of the system and the phase is the position angle of the system on the sky. The abscissa of the plot is the position angle in the  $x$ - $y$  system, which is equal to the values listed in Table 1 minus  $1.41^\circ$  (which accounts for the rotation to align the spectra with the  $y$ -axis). Fig. 6 shows the definitions of the different angles used in the analysis, and their relations to one another.

## 5.5 Weights

The non-linear least squares involves fitting an array which consists three sets of centroids and the *IUE* fluxes all at once. To perform the fit, we must provide errors for the different components of this array. The measurement errors affecting the centroids were obtained from the s.d. of the three independent sets of measurements obtained at each offset position. For the *IUE* data, we used the error vector which accompanies the MXLO fluxes (see Nichols & Linsky 1996).

## 6 RESULTS

In fitting the data, we assumed a microturbulent velocity of  $2.0 \text{ km s}^{-1}$ , which is typical for main sequence B stars (e.g. Fitzpatrick & Massa 2005). Because the B star is overwhelmed

<sup>1</sup> We use the Markwardt non-linear IDL fitting procedure, available at <http://astro.physics.wisc.edu/~craigm/idl/idl.html>

<sup>2</sup> We used the Kurucz ‘preferred models’ available at <http://kurucz.harvard.edu/>

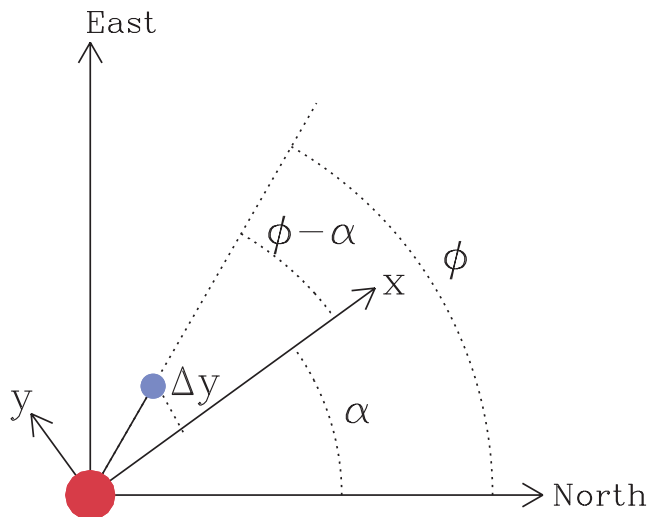


**Figure 6.** Diagram showing the definitions of the different angles and coordinate systems used in the analysis, and their relations to one another. The position angle on the sky of the binary angle,  $\phi$ , is defined as the angle measured c.c. from north to east, with the primary at the origin. The  $x$ - $y$  system is the standard STIS coordinate system, with  $x$  parallel to the dispersion (increasing in the direction of increasing wavelength) and  $y$  perpendicular to it. The angle  $\alpha$  (also measured c.c. from north to east) is defined as the angle between north and  $x$  for a given telescope orientation. Thus,  $\phi - \alpha$  is the angle between the dispersion and a line connecting the binary components, and  $\Delta y = \theta \sin(\phi - \alpha)$  is the displacement of the two spectra of the binary perpendicular to the dispersion. If  $\phi - \alpha = 0$  or  $\pm 180^\circ$ , then  $\Delta y = 0$ .

by the Cepheid in the optical and near-UV, we do not have access to the classical  $\log g$  diagnostics for B stars, namely, the Balmer jump and Balmer lines. Consequently, we fixed the surface gravity at 4.0, again typical for main-sequence B stars. We allowed the abundance parameter,  $[m/H]_s$ , and the effective temperature of the B star to be optimized by the least squares routine, along with the  $\Delta y$ s and the extinction parameters. In addition, we assumed that the *IUE* fluxes were correct (so the STIS fluxes were divided by 1.146 to make them agree with the *IUE* data). In applying our model, we also assume that all of the STIS flux in a 30-Å band centred at 1650 Å is due to the B star. We shall examine the effects of our assumptions shortly. Only the *IUE* fluxes between 1250 and 1700 Å are incorporated into the fit of the SED, which constrains the physical properties of the B star. This extends slightly beyond the 1650 Å limit used for the STIS data, but recall that the *IUE* data were obtained when the Cepheid was near minimum light, and nearly a factor of 2 fainter in the UV (see Fig. 4).

The parameters determined from the fit are given in Table 2, where parameters that were fixed in the fit are enclosed in parentheses. Fig. 7 shows our fits to the centroids. The points are the observed data and the solid curves are the fits obtained simultaneously with the fit to the fluxes. The effects of spectral features on the centroids are clearly seen. Fig. 8 shows the fit to the SED below 1650 Å. We do not show the fit to the binary SED longward of 1650 Å since it is, by definition, exact. The extinction curve derived from the best fit is also shown in Fig. 8, where it is compared to a standard  $R_V = 3.1$  curve from Fitzpatrick (1999).

We can also estimate the physical parameters of the Cepheid component of the binary by fitting its mean SED inferred from fit. This SED is found by subtracting the reddened B star model from

**Table 2.** Parameter values.

Parameter	Value	Parameter	Value
$\Delta y_1$	−0.010	$c_3$	4.13
$\Delta y_2$	0.279	$c_4$	0.82
$\Delta y_3$	−0.269	$\gamma$	0.9686
$T_{\text{eff}}^p$	[6297]	$V_s$	(11.084)
$T_{\text{eff}}^s$	15735	$(B - V)_0^s$	(−0.156)
$\log g_p$	(4.00)	$(U - B)_0^s$	(−0.597)
$\log g_s$	[1.60]	$V_p$	(7.362)
$[m/H]_p$	[0.00]	$(B - V)_0^p$	(0.494)
$[m/H]_s$	−0.20	$(U - B)_0^p$	(0.359)
$E(B - V)$	0.53	$\Delta \log L$	(0.95)
$R(V)$	3.11		

Values in parentheses were not involved in the fitting procedure. Values in square brackets were determined from a fit to the Cepheid SED derived from the initial fit.

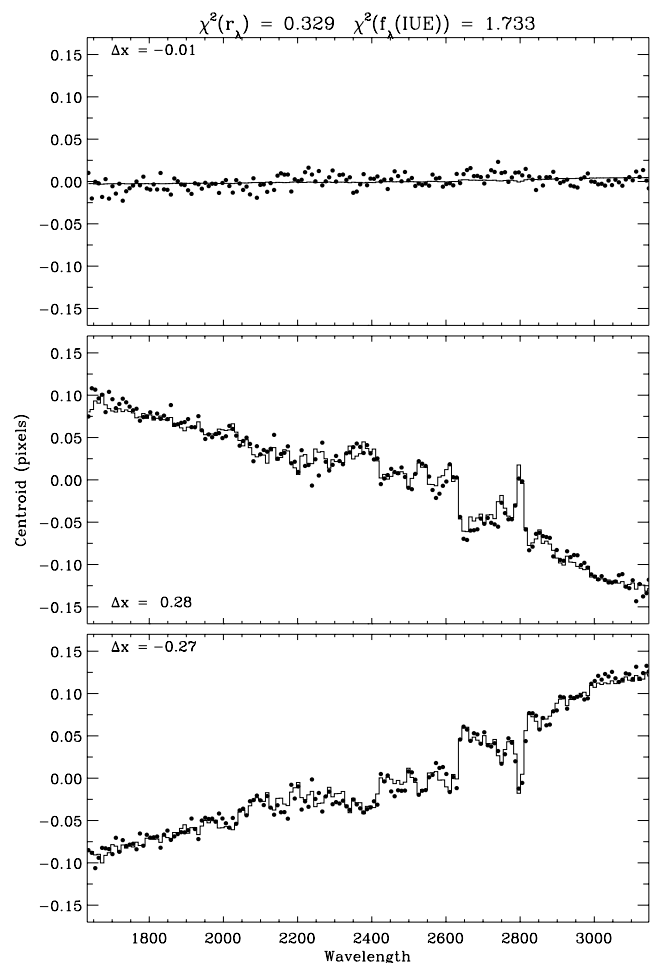


**Figure 7.** Fits to the mean centroids at each roll angle for AW Per. Each mean centroid was fit simultaneously with the corresponding fluxes, optical photometry and interstellar extinction. A Kurucz model was used to fit the B star component, and the Cepheid flux was taken to be the difference between the reddened B star model and the observed flux.

the observed SED of the system and then correcting this difference for the effects of extinction. The unreddened SED plus its  $V$ ,  $(B - V)_0$  and  $(U - B)_0$  (also inferred from the fit) were then fit to an Atlas 9 model. The  $V$ ,  $(B - V)$  and  $(U - B)$  photometry were initially assigned errors of 0.02, 0.01 and 0.02 mag, respectively. In

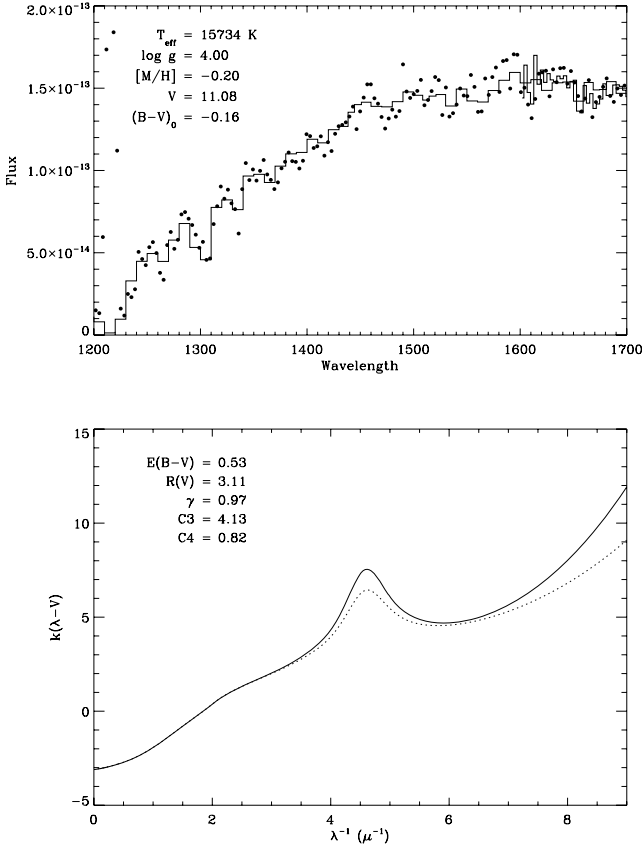


**Figure 8.** Top: best-fitting B star (thin curve) compared to the *IUE* (points) and STIS (the curve from 1600 to 1700 Å) fluxes. The model includes reddening. We only show the far-UV region, since the fit is, by definition, exact for wavelengths longward of 1650 Å. Bottom: AW Per extinction curve determined by the simultaneous fit of the flux and centroids (solid curve) compared to a standard  $R_V = 3.1$  curve (dotted) from Fitzpatrick (1999).

performing this fit, we fixed the microturbulent velocity at  $2 \text{ km s}^{-1}$ , and allowed  $T_{\text{eff}}^p$  (the effective temperature of the primary),  $\log g_p$  (the surface gravity of the primary) and  $[M/H]_p$  (the abundance of the primary), to vary. We had to restrict the surface gravity to be larger than 1.6, otherwise the fitting routine would seek  $\log g_p$  values that were unrealistically small (we expect a  $\log g_p \simeq 2.0$ ; e.g. Evans 1994). Furthermore, we had to increase the weight (decrease the error) of the  $(B - V)$  photometry by a factor of 10 in order to obtain reasonable agreement with the photometry. Fig. 9 compares the unreddened SED of the Cepheid to the best-fitting model. The parameters derived from the fit are also listed in Table 2 and are enclosed in square brackets, to distinguish them from the parameters derived from the initial fit to the data.

It is also possible to test the reasonableness of the inferred UV Cepheid SED by comparing it to *IUE* observations of the single Cepheid star  $\delta$  Cep.  $\delta$  Cep has a period of 5.4 d, compared to 6.5 d for AW Per, and its mean unreddened colour is  $\langle(B - V)\rangle = 0.57$ . To obtain the intrinsic colour of AW Per, we use our derived colour excess for the system and the intrinsic colours of the B star secondary from Table 2 and the mean magnitude of the system,  $\langle V \rangle = 7.49$  mag, to correct the observed mean colour of the system,  $\langle(B - V)\rangle = 1.06$  mag, for both extinction and the presence of the companion. The result is  $\langle(B - V)_0^p\rangle = 0.57$ , identical to that of  $\delta$  Cep (recall that the intrinsic colour we derive for AW Per is at  $\Phi \simeq 0.92$ ). Thus, the comparison between these two stars is expected to be

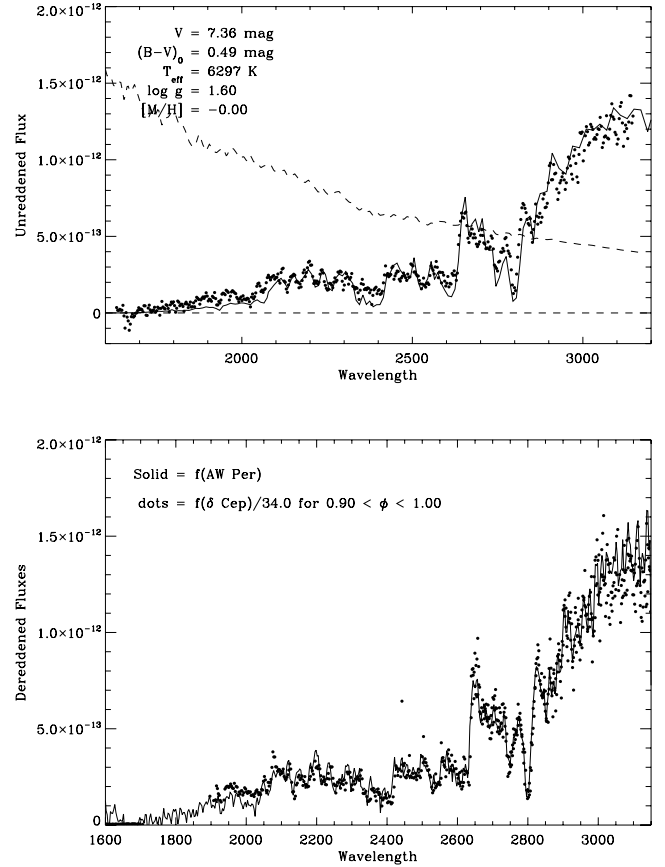


**Figure 9.** Top: inferred dereddened Cepheid SED (points) compared to the best-fitting Kurucz model (solid) and the dereddened flux of the best-fitting B star (dashed). Bottom: comparison of the unreddened Cepheid flux (solid curve) and an unreddened *IUE* spectrum (dots) of  $\delta$  Cep observations for  $0.90 \leq \Phi \leq 0.95$ . The  $\delta$  Cep flux is scaled by the difference between  $V = 3.54$  at  $\Phi = 0.925$  for  $\delta$  Cep and  $V = 7.37$ , the magnitude of the primary in AW Per at  $\Phi = 0.92$  (the mean phase of the STIS observations). As discussed in the text, the  $\delta$  Cep spectrum is a combination of several *IUE* spectra.

quite good. The bottom plot in Fig. 9 compares the unreddened *IUE* data (points) for  $\delta$  Cep from several exposures obtained for  $0.9 \leq \Phi(\delta \text{ Cep}) \leq 1.0$  to the unreddened Cepheid STIS spectrum (solid curve) of AW Per. Several *IUE* exposures are required to produce the  $\delta$  Cep spectrum since the dynamic range of *IUE* was so limited and the range of the UV SED of  $\delta$  Cep is so large. The *IUE* data had the Massa & Fitzpatrick (2000) corrections applied, were dereddened by an  $E(B - V) = 0.09$  (Dean, Warren & Cousins 1987) and scaled by  $10^{-0.4(7.37-3.54)}$ , which corresponds to magnitude difference of AW Per at  $\Phi = 0.92$  (the mean for the STIS data) and  $\delta$  Cep at  $\Phi = 0.95$  (the mean of the *IUE* data).

Finally, we utilize the  $\Delta y^{(m)}$  which resulted from the fits to derive the separation of the system and its position angle on the sky. These are found by fitting equation (2) to the plot of  $\Delta y$  versus roll angle shown in Fig. 10. The error bars at each orientation are the quadratic mean errors for that roll determined from the dispersion in the fits to the three individual sets of observations obtained at each orientation (see next section). The inverse of the errors squared were used to weight the fit. The final result of the analysis is a separation of  $\theta = 13.74 \pm 0.26$  mas and a position angle  $\phi = 184^\circ.16 \pm 1^\circ.94$ , for an accuracy of  $\sim 2$  per cent.



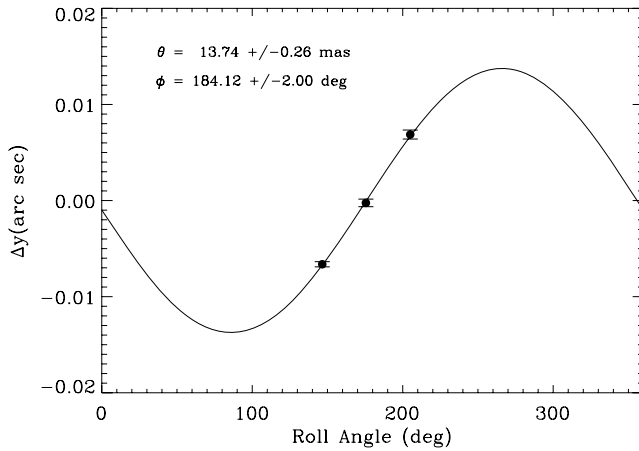


**Figure 10.** Determination of the angular separation of AW Per. The observational errors for  $\Delta y$  were determined from individual fits to the three independent offset observations at each roll angle.

**Table 3.** Errors.

Param.	Prog.	s.d.	$ \delta \log g $	$ \delta \frac{f_{IUE}}{f_{STIS}} $	$ \delta \frac{f_s}{f_p + f_s} $
$\Delta y^{(1)}$	0.004	0.015	$1.4 \times 10^{-4}$	$6.5 \times 10^{-6}$	$5.0 \times 10^{-4}$
$\Delta y^{(2)}$	0.005	0.017	0.0019	$1.4 \times 10^{-4}$	0.015
$\Delta y^{(3)}$	0.005	0.014	0.0021	$1.3 \times 10^{-4}$	0.015
$T_{\text{eff}}^s$	248	105	1205	9.1	37
$[m/H]_s$	0.057	0.025	$7.5 \times 10^{-5}$	0.0016	0.0064
$E(B - V)$	0.001	0.038	0.018	0.0026	0.038
$R_V$	0.031	0.12	0.11	0.0090	$2.7 \times 10^{-4}$
$\gamma$	0.015	$2.4 \times 10^{-4}$	0.019	$8.6 \times 10^{-4}$	0.0025
$c_3$	0.14	0.32	0.049	0.029	0.0055
$c_4$	0.019	0.066	0.014	$4.3 \times 10^{-3}$	0.0068

### 6.1 Errors in the parameters

In this section, we describe the internal, random, errors affecting our parameter determinations, and also examine the influence of systematic effects upon the results.

The random errors were evaluated in two, independent ways. One is the error estimates calculated by the least squares routine, which are determined by evaluating derivatives of the model. These errors are listed in the second column of Table 3. We also obtained error estimates by fitting the sets of observations obtained at the same offset at each roll angle, independently. These provide three sets of independent observations and we used the parameters determined from each set to obtain standard deviations (s.d.) of the model parameters. These estimates (divided by  $\sqrt{3}$  applicable to the error in the mean) are listed in the third column of Table 3. Notice that the errors in the  $\Delta y^{(n)}$  determined from the s.d. are nearly twice as large. To be conservative, these errors were used as the error shown in Fig. 10 and in determining the errors in  $\theta$  and  $\phi$ .

Beside the random (or measurement) errors, systematic effects will also be present. We characterize these by varying the different assumptions which enter the fitting procedure, and then examining their influence on the result. To begin, we varied the assumed value of  $\log g$  used to fit the B star by  $\pm 0.5$ , which should encompass all plausible values. The result (the difference divided by 2) is listed in column 4 of Table 3. Next, we tested the affect of assuming that the STIS (and not the IUE) fluxes are correct and allowed for the possibility that the B star accounts for only 95 per cent, instead of

100 per cent of the flux at 1650 Å. These results are listed in the last two columns of Table 3.

As can be seen from Table 3, the varying the  $\log g$  can cause a significant change in  $T_{\text{eff}}^s$ , but has little effect on the  $\Delta y^{(n)}$ , which are the object of our analysis. In fact, the only significant change in the  $\Delta y^{(n)}$  result from our inability to determine whether the STIS or IUE fluxes are correct, and even these errors are only of the same order of the errors determined from the repeated observations. As a result, we conclude that the angular separation determined from our analysis is very robust to variations in the assumptions or input parameters.

## 7 DISCUSSION

We have seen that the separation determined from the fit is quite stable. We now discuss the physical parameters determined from our fits (Table 2), their reliability and their implications.

We first consider the Cepheid SED derived from the fit. It is compared to the best-fitting Atlas 9 model in top panel of Fig. 9. This ‘best-fitting model is not a very good fit, since it lies systematically below the observed flux in far-UV flux and over it in the near-UV flux. Furthermore, the agreement with the optical photometry is not very good. The model predicts  $V = 7.362$ ,  $(B - V) = 0.470$  and  $(U - B) = 0.309$ . The agreement with the  $(B - V)$  colour given in Table 2 is fair, but recall that it was given a very large weight. The agreement with the inferred  $(U - B)$  is not very good at all. The poor overall fit probably results from the shortcomings of Atlas 9 models for Cepheids discussed below.

The bottom panel of Fig. 9 compares the unreddened SED of the Cepheid component of AW Per to the unreddened SED of the single Cepheid,  $\delta$  Cep at approximately the same phase. This figure demonstrates three points. First, the two SEDs agree surprising well. Secondly, the strong far-UV flux in the derived SED relative to the models is also present (and slightly larger) in  $\delta$  Cep, so the derived SED is quite reasonable. Thirdly, the flux in  $\delta$  Cep is extremely small for wavelengths shortward of 1650 Å, bolstering our assumption that all of the flux in AW Per observed below 1650 Å is due to the B star secondary.

So, why is the Atlas 9 model fit of the Cepheid so poor? One must remember that Cepheid UV SEDs depend on numerous, ill-defined physical processes that are not fully incorporated into the Atlas 9 models. These include spherical extension, which can enhance the UV flux from an atmosphere (see fig. 4 in Hauschildt et al. 1999), chromospheres (e.g. Sasselov & Lester 1994), the amount of convective energy transport (Castelli, Gratton & Kurucz 1997) and the details of the line blanketing (Prieto, Lambert & Lambert 2003). In addition, there are inevitably dynamical effects that are not treated by the models.

In fact, we initially attempted to fit the data with using an approach that employed models for both the Cepheid and the B star. However, we abandoned it because it produced poor fits and the separations that were  $\sim 10$  per cent larger than those derived from the adopted technique. The origin of the systematic difference in the centroids can be traced to the gradient in the flux residuals seen in the top of Fig. 9. These propagate into the fits of the centroids. Perhaps the use of more detailed Cepheid models could solve this problem.

In spite of these difficulties, it is of interest to examine the physical parameters determined from the Cepheid model. To begin,  $T_{\text{eff}}$  of the best-fitting model agrees reasonably well with previous estimates for Cepheid temperatures near maximum light (Evans & Teays 1996; Fry & Carney 1999; Kovtyukh & Gorlova 2000). On

the other hand, the fit selects a very low surface gravity and would have settled on an even lower value if it had been allowed to do so. It is also interesting that the Cepheid model has a significantly different metallicity than the B star. However, this may not be too strange. Instead, it may simply reflect the fact that the  $[M/H]$  parameter in cooler models responds more to spectral features produced by CNO elements, while the same parameter in the B stars responds to the Fe abundance (Fitzpatrick & Massa 1999).

Next, we consider the parameters determined for the B star. The model fit to the far-UV (Fig. 8) is quite good, and the extinction curve, while distinctly different from the canonical  $R_V = 3.1$  curve, is rather unremarkable, with parameters well within normal bounds (e.g. Fitzpatrick & Massa 1990; Valencic, Clayton & Gordon 2004). Also, the  $[M/H]$  for the B star is well within the expected range for such stars (e.g. Fitzpatrick & Massa 1999, 2005) and the inferred colour excess is quite close to previous determinations (Evans 1994). It should not be surprising that these fits are so good, since both the extinction model and the ability of the Atlas 9 models to describe normal B star spectra are well documented. Notice that  $T_{\text{eff}}$  we derive is considerably hotter than previously estimated by Evans (1994), and lies somewhat closer to the ZAMS (see fig. 7 in Evans 1994). However, its probable mass,  $\sim 5 M_{\odot}$  (based on its  $T_{\text{eff}}$ ; Andersen 1991), remains significantly less than the lower limit of  $\sim 6.6 M_{\odot}$  determined from the radial velocity orbit of the primary by Evans et al. (2000). Thus, it still appears likely that the B star component of AW Per must also be a binary.

## 8 SUMMARY

We have shown that the signatures of the Cepheid and B star components of AW Per are clearly present in the wavelength dependence of the centroid of its spectrum. This result demonstrates the power of our approach. A simple model was devised to extract the angular separation of the binary from the centroid measurements. The accuracy of the angular separation is  $\sim 2$  per cent, or  $\pm$  a few  $\times 10^{-4}$  arcsec! We also demonstrated that the results are extremely stable to variations in the expected systematic effects in the data and its analysis. We also showed that one possible source of uncertainty in the current data is the absolute level of the far-UV data. Higher quality far-UV observations to secure the B star flux level and secure its parameters would be extremely useful.

Our final results are listed in Table 2. In addition to the angular separations and position angle, these include a Cepheid temperature and systemic extinction that agree with previous estimates and a B star secondary temperature that is considerably hotter than previously thought (e.g. Evans 1994). However, the likely mass of the secondary still appears too small to account for the minimum mass of the secondary inferred by the radial velocity of the primary. Consequently, it is likely that the B star component of AW Per is also be a binary.

Finally, the long period of AW Per's orbit means that it will be a few years before the separation changes enough for the second independent observation needed to determine  $\sin i$  can be obtained.

## ACKNOWLEDGMENTS

We would like to thank Karla Peterson and Charles Proffitt of STScI, who provided valuable guidance in preparing the observations. This work was supported by NASA grants to SGT, Inc. and SAO.

## REFERENCES

- Andersen J., 1991, *A&AR*, 3, 91  
 Beckers J. M., 1982, *Opt. Acta*, 29, 361  
 Benedict G. F. et al., 2002, *AJ*, 124, 1695  
 Castelli F., Gratton R. G., Kurucz R. L., 1997, *A&A*, 318, 841  
 Dean J. F., Warren P. R., Cousins A. W. J., 1987, *MNRAS*, 183, 569  
 Evans N. R., 1989, *AJ*, 97, 1737  
 Evans N. R., 1994, *ApJ*, 436, 273  
 Evans N. R., 1995, *ApJ*, 445, 393  
 Evans N. R., Teays T. J., 1996, *AJ*, 112, 761  
 Evans N. R., Bohm-Vitense E., Carpenter K., Beck-Winchatz B., Robinson R., 1998, *ApJ*, 494, 768  
 Evans N. R., Vinko J., Wahlgren G. M., 2000, *AJ*, 120, 407  
 Evans N. R. et al., 2007, in Hartkopf W. I., Guinan E. F., Harmanec P., eds, *Proc. IAU Symp. 240, Binary Stars as Critical Tools and Tests in Contemporary Astrophysics*, Cambridge Univ. Press, Cambridge, p. 102  
 Fitzpatrick E. L., 1999, *PASP*, 111, 63  
 Fitzpatrick E. L., Massa D., 1990, *ApJS*, 72, 163  
 Fitzpatrick E. L., Massa D., 1999, *ApJ*, 525, 1011  
 Fitzpatrick E. L., Massa D., 2005, *AJ*, 129, 1642  
 Fry A. M., Carney B. W., 1999, *AJ*, 118, 1806  
 Groenewegen M. A. T., Oudmaier R. D., 2000, *A&A*, 356, 849  
 Hauschildt P. H., Allard F., Ferguson J., Baron E., Alexander D. R., 1999, *ApJ*, 525, 871  
 Kervella P., Fouqué P., Storm J., Gieren W. P., Bersier D., Mourard D., Nardetto N., Foresto V., 2004, *ApJ*, 604, L113  
 Kim Quijano J. et al., 2003, *STIS Instrument Handbook*, Version 7.0. STScI, Baltimore  
 Kiss L. L., 1998, *MNRAS*, 297, 825  
 Kovtyukh V. V., Gorlova N. I., 2000, *A&A*, 358, 587  
 Kurucz R. L., 1991, in Crivellari L., Hubeny I., Hummer D. G., eds, *NATO ASI Ser. C., Stellar Atmospheres: Beyond Classical Models*. Kluwer, Dordrecht, p. 441  
 Lindler D., 1998, *CALSTIS Reference Guide*, CALSTIS Version 5.1. GSFC, Greenbelt, MD  
 Massa D., Endal A. S., 1987, *AJ*, 93, 579  
 Massa D., Fitzpatrick E. L., 2000, *ApJS*, 126, 517  
 Moffett T. J., Barnes T. G., 1984, *ApJS*, 55, 389  
 Nichols J. S., Linsky J. L., 1996, *AJ*, 111, 517  
 Porter J. M., Oudmaier R. D., Baines D., 2004, *A&A*, 428, 327  
 Prieto C. A., Hubeny I., Lambert D. L., 2003, *ApJ*, 591, 1192  
 Romaniello M., Primas F., Mottini M., Groenewegen M., Bono G., Franois P., 2005, *A&A*, 429, L37  
 Sasselov D. D., Lester J. B., 1994, *ApJ*, 423, 795  
 Schaller G., Schaerer D., Meynet G., Maeder A., 1992, *A&AS*, 96, 269  
 Schmidt G. S., Parsons S. B., 1982, *ApJS*, 48, 185  
 Simon N. R., 1990, in Cacciari C., Clementini G., eds, *ASP Conf. Ser. Vol. 11, Confrontation between stellar pulsation and evolution*. Astron. Soc. Pac., San Francisco, p. 193  
 Szabados L., 1980, *Commun. Konkoly Obs. Hung. Acad. Sci., Budapest*, No. 76  
 Szabados L., 1991, *Commun. Konkoly Obs. Hung. Acad. Sci., Budapest*, No. 96  
 Valencic L. A., Clayton G. C., Gordon K. D., 2004, *ApJ*, 616, 912

## APPENDIX A: MATHEMATICAL DETAILS

This appendix provides a detailed derivation of how the wavelength dependence of the centroid of the dispersed image can be used to determine the separation of a binary whose components have different colours.

Consider the set of angular coordinates  $x$  and  $y$  which are parallel and perpendicular to the dispersion, respectively, with  $x$  increasing in the direction of increasing wavelength (this is the standard STIS coordinate system; Kim Quijano et al. 2003). Now, let  $h(y)$  be the instrumental profile in the cross-dispersion direction,  $y$ . Then the

spectrum of a single star located at  $y = y_0$  can be expressed as

$$f(\lambda, y) = N(\lambda)h(y - y_0), \quad (\text{A1})$$

where  $\lambda = \lambda(x)$ , and  $N(\lambda)$  is the photon flux at  $\lambda$  (we assume infinite resolution in the wavelength direction).

If the spectra of the primary and secondary components of the binary are centred at  $y_p$  and  $y_s$ , then their spectra are separated by  $\Delta y = y_s - y_p$ , and the image of the binary spectrum is given by

$$f(\lambda, y) = N_p(\lambda)h(y - y_p) + N_s(\lambda)h(y - y_p - \Delta y). \quad (\text{A2})$$

If  $\Delta y$  is small compared to structure in  $h(y)$ , this equation can be approximated by

$$\begin{aligned} f(\lambda, y) &\simeq N_p(\lambda)h(y - y_p) \\ &\quad + N_s(\lambda) \left[ h(y - y_p) + \Delta y \frac{dh(y)}{dy} \Big|_{y=y-y_p} \right] \\ &= [N_p(\lambda) + N_s(\lambda)] \\ &\quad \times \left[ h(y - y_p) + \frac{N_s(\lambda)}{N_p(\lambda) + N_s(\lambda)} \Delta y \frac{dh(y)}{dy} \Big|_{y=y-y_p} \right] \\ &\simeq [N_p(\lambda) + N_s(\lambda)] \\ &\quad \times h \left[ y - \left( y_p + \frac{\Delta y N_s(\lambda)}{N_p(\lambda) + N_s(\lambda)} \right) \right]. \end{aligned} \quad (\text{A3})$$

Therefore, the wavelength dependence of the centroid of the spectrum will vary as

$$y(\lambda) = y_p + \frac{\Delta y N_s(\lambda)}{N_p(\lambda) + N_s(\lambda)} = y_p + \frac{\Delta y}{1 + R(\lambda)}, \quad (\text{A4})$$

where  $R(\lambda) = N_p(\lambda)/N_s(\lambda)$  is the flux ratio of the binary components.

Now, the separation  $\Delta y$  depends on both the separation of the binary,  $\theta$ , and the orientation of the system relative to the dispersion

direction. The position angle on the sky of the binary,  $\phi$ , is defined as the angle measured c.c. from north to east, with the primary at the origin. The angle  $\alpha^{(n)}$  (also measured c.c. from north to east) is defined as the angle of a line in the dispersion direction pointing in the direction of increasing wavelength for the  $n$ th telescope orientation. In this case,  $\phi - \alpha^{(n)}$  is the angle between the dispersion and a line connecting the binary components and  $\Delta y^{(n)} = \theta \sin(\phi - \alpha^{(n)})$  is the displacement of the two spectra of the binary (note that when  $\phi - \alpha = 0, \pm 180^\circ$ ,  $\Delta y = 0$ ). Therefore, the observation obtained with the telescope in the  $n$ th orientation can be expressed as

$$y(\lambda)^{(n)} = y_p^{(n)} + \theta \sin(\phi - \alpha^{(n)}) [1 + R(\lambda)]^{-1}, \quad (\text{A5})$$

where  $y_p^{(n)}$  is the wavelength-independent displacement of the  $n$ th exposure in  $y$ .

To extract both  $\theta$  and  $\phi$  from the observed centroids, at least two observations at different  $\alpha$ s are required. Therefore, as long as the relative fluxes of the binary components are known, a linear regression of the wavelength dependence of the centroid against  $[1 + R(\lambda)]^{-1}$  gives  $\Delta y^{(n)}$  for that observation. The  $y_p^{(n)}$  are constant terms related to the absolute position of the primary star, although in practice they cannot be reliably disentangled from the large random errors in the absolute position of the binary on the detector at each orientation.

Once the  $\Delta y^{(n)}$  are determined for each orientation, these are plotted against the known quantities,  $\alpha^{(n)}$ . Since

$$\Delta y^{(n)} = \theta \sin(\phi - \alpha^{(n)}) \quad (\text{A6})$$

fitting a sine function to the  $\Delta y^{(n)}$  as a function of the  $\alpha^{(n)}$  determines  $\phi$  and  $\theta$ , the observables of an astrometric binary at the epoch of the observations.

This paper has been typeset from a  $\text{\LaTeX}$  file prepared by the author.